Journal of Computational Physics 228 (2009) 2132–2151

Contents lists available at ScienceDirect

Journal of Computational Physics

journal homepage: www.elsevier.com/locate/jcp

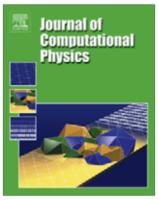

Deformation of elastic particles in viscous shear flow

Tong Gao, Howard H. Hu *

Department of Mechanical Engineering and Applied Mechanics, University of Pennsylvania, Philadelphia, PA 19104, USA

ARTICLE INFO

Article history:
Received 25 July 2008
Received in revised form 17 October 2008
Accepted 24 November 2008
Available online 9 December 2008

Keywords:
Fluid–structure interactions
Eulerian *Almansi* strain tensor
Elastic particle deformation
Particle–particle interactions
Finite elements

ABSTRACT

In this paper, the dynamics of two dimensional elastic particles in a Newtonian viscous shear flow is studied numerically. To describe the elastic deformation, an evolution equation for the Eulerian *Almansi* strain tensor is derived. A constitutive equation is thus constructed for an incompressible "Neo–Hookean" elastic solid where the extra stress tensor is assumed to be linearly proportional to the *Almansi* strain tensor. The displacement field does not appear in this formulation. A monolithic finite element solver which uses Arbitrary Lagrangian–Eulerian moving mesh technique is then implemented to solve the velocity, pressure and stress in both fluid and solid phase simultaneously. It is found that the deformation of the particle in the shear flow is governed by two non-dimensional parameters: Reynolds number (Re) and Capillary number (Ca, which is defined as the ratio of the viscous force to the elastic force). In the Stokes flow regime and when Ca is small ($Ca < 0.65$), the particle deforms into an elliptic shape while the material points inside the particle experience a tank-treading like motion with a steady velocity field. The deformation of the elastic particle is observed to vary linearly with Ca, which agrees with theoretical results from a perturbation analysis. Interactions between two particles in a viscous shear flow are also explored. It is observed that after the initial complicated interactions, both particles reach an equilibrium elliptic shape which is consistent with that of a single particle.

1. Introduction

In a solid–liquid suspension, interactions between the solid particulates and the viscous liquid determine the rheological behavior of the suspension. It is known that the clusters and anisotropic particle micro-structures are the result of particle migrations produced by particle–particle and particle–wall interactions [1–3]. When solid particles are deformable, the elasticity of particles may induce more complicated fluid–solid interactions which largely affects the behaviors of the mixture. Generally, elastic particles are deformed by viscous stresses from the bulk fluid. The extent of the deformation depends on the applied hydrodynamic force intensity on the particle surface, particle geometry and material properties of elastic particles. In the past decades, there has been an increasing interest in the dynamics of mesoscopic deformable objects in a viscous fluid flow [4–6], particularly with applications in biological systems where a number of cases can be characterized by fluid–structure interactions.

A well-known example of the fluid–structure interaction at mesoscopic scale is the dynamics of fluid vesicles in a viscous shear flow. A fluid vesicle (or capsule) is a particle with a lipid membrane which encloses a liquid drop [4]. Such a particle can deform when freely suspended in a viscous shear flow due to the coupling of the elasticity of the membrane, the constant volume and surface area, as well as the hydrodynamic forces within and outside the membrane. The mechanisms of vesicle deformations are also helpful to understand the basic physical aspects of the complicated biological cells. For example, the

---

* Corresponding author. Tel.: +1 215 898 8504; fax: +1 215 573 6334.
E-mail address: hhu@seas.upenn.edu (H.H. Hu).

0021-9991/$ - see front matter © 2008 Elsevier Inc. All rights reserved.
doi:10.1016/j.jcp.2008.11.029

red blood cell (RBC) can be regarded as a biconcave discoid vesicle with a bilayer of lipids into which proteins are embedded. The behavior of the RBC in viscous shear flows has been investigated extensively in medical applications [21,22]. Theoretical works [23–25] have shown that the vesicle experiences either a steady ellipsoidal tank-treading motion or an unsteady flipping motion, depending on different physical properties and flow conditions. On the other hand, numerical simulations and analysis have also been performed to solve dynamics of vesicles with large deformations. For example, Eggleton and Popel [26] employed an immersed boundary method to simulate asymptotic behaviors of RBC in a simple shear flow with an increasing ratio of the dilation modulus to the extensional modulus. At vanishing Reynolds numbers, Pozrikidis and co-workers [27–29] used a boundary element method to study transient deformations of vesicles with various shapes and membrane properties in simple shear flow. Recently, a hybrid method which incorporate the immersed boundary concept into the lattice Boltzmann method with a multi-block mesh refinement strategy is used by Sui et al. [30] to study spherical vesicles deforming in a shear flow at both small and moderate Reynolds numbers.

Besides experimental and theoretical approaches, there are extensive works in developing efficient numerical methods to simulate interactions between fluid and elastic objects. In general, these methods can be roughly classified into two categories: non-boundary conforming methods and boundary conforming methods. The non-boundary conforming methods employ a mixture of Eulerian and Lagrangian descriptions. The Navier–Stokes (N–S) equations are solved on a fixed Eulerian mesh, while the embedded boundaries are tracked by a set of freely moving Lagrangian points. To account for the no-slip conditions at fluid–solid interfaces, appropriate forcing density terms are added to the N–S equations by using proper interpolations between the solution variables at the fixed grid points in the vicinity of the moving boundary and the nearest Lagrangian points[7–11]. This treatment greatly simplifies the mesh generation, and simulates moving boundaries in a more straightforward manner [12]. However, the interpolation between the moving boundary and the fixed grid will inevitably introduce additional numerical errors which usually lower the accuracy of the solution. Moreover, the conditions at the fluid–solid interface are not exactly satisfied in these methods.

On the other hand, only one mesh set is used in the boundary conforming methods, adapting to the complex geometries of the deforming and/or moving objects. The governing equations are solved on the moving mesh conformed to the fluid–solid boundary movement. Two widely used techniques are the Arbitrary Lagrangian–Eulerian (ALE) technique [13] and the space-time finite element method [14]. For fluid–structure interactions, it is common to use one solver for the N–S equations in the fluid phase and another for the solid phase, and iterate between them until the solution converges [15–18]. The iterative strategies usually employ either loose coupling partitioned algorithms [15,16] or strong coupling up to simultaneous solutions [17,18]. In both methods, subiteration can be performed for better convergence. For particulate flows with deformable objects undergoing large deformations, however, the loose coupling partitioned algorithms may be difficult to converge due to the very strong fluid–structure interactions [19]. For strong fluid–structure interactions, robust simultaneous solution procedures are needed to ensure the stability and convergence of the time accurate coupled solutions [19,20].

In the present paper, we develop a new finite element method to solve the dynamics of two-dimensional (2D) elastic particles deforming in a viscous shear flow, which is governed by the Reynolds number and the Capillary number. Different from the capsules, here the solid particles are assumed to be bulk elastic objects consisting of the ‘‘Neo–Hookean” material. This method can be extended to deal with vesicles with an elastic membrane of finite thickness. In comparison with the previous treatments, the Eulerian *Almansi* strain tensor is introduced to describe the elastic deformations. Thus, the unknown variables in both fluid and solid phase are the velocity, pressure and stress, and the displacement field does not appear in the formulation. By using an Arbitrary Lagrangian–Eulerian (ALE) finite element formulation, we then implement a monolithic solver to solve two of the phases simultaneously. In this method, consistent time integration schemes and discretizing methods can be employed for all physical variables, eventually leading to a linear system which can be solved by efficient iterative schemes with appropriate preconditioners.

The paper is organized as follows. In Section 2, we first derive an evolution equation for the Eulerian *Almansi* strain tensor. For the ‘‘Neo–Hookean” elastic material, a constitutive equation is then established by assuming that the extra stress tensor is linearly proportional to the *Almansi* strain tensor. Next, we use an ALE finite element weak formulation for the governing equations. In Section 3, both single particle deformation and particle–particle interactions in a Newtonian viscous shear flow are investigated numerically. A perturbation analysis is also performed to characterize the single particle deformation in the limit of small Capillary number. The results of the work are summarized in Section 4.

2. Mathematical formulation and numerical algorithm

Consider the deformation of a 2D elastic particle suspended in an incompressible Newtonian viscous fluid which is confined between two parallel plates as shown in Fig. 1. An initially circular elastic particle with diameter d_p is placed at the center of the channel. The solid particle is assumed to be incompressible and neutrally buoyant. The width of the channel is H and the length is $2H$. The upper and bottom walls are moving in the opposite directions with the same velocity U. Thus, the shear rate of the flow is $\dot{\gamma} = 2U/H$.

The fluid flow is governed by the N–S equations

$$\nabla \cdot \mathbf{v}_f = 0, \tag{1}$$

$$\rho_f \left(\frac{\partial \mathbf{v}_f}{\partial t} + (\mathbf{v}_f \cdot \nabla)\mathbf{v}_f \right) = \nabla \cdot \boldsymbol{\sigma}_f, \tag{2}$$

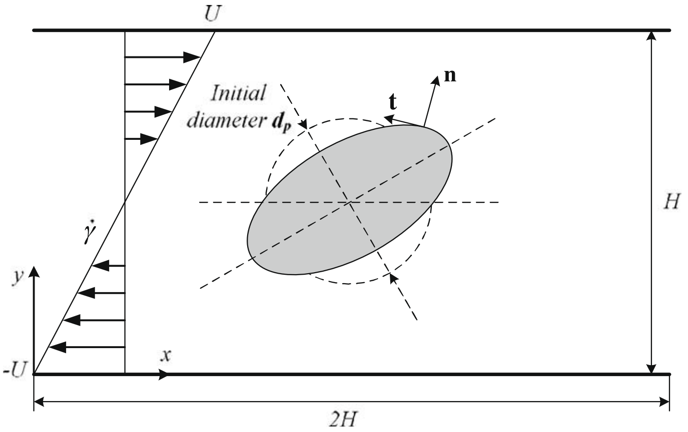

Fig. 1. Schematic for an elastic particle deforming in a viscous shear flow bounded by two moving walls.

where $\mathbf{v}_f$ is the fluid velocity, ρ_f is the fluid density, and $\boldsymbol{\sigma}_f$ is the stress tensor defined as

$$\boldsymbol{\sigma}_f = -p_f\mathbf{I} + \boldsymbol{\tau}_f = -p_f\mathbf{I} + \mu_f[\nabla\mathbf{v}_f + (\nabla\mathbf{v}_f)^T], \tag{3}$$

where p_f is the pressure, $\boldsymbol{\tau}_f$ is the extra stress tensor in the fluid, and μ_f is the dynamic viscosity.

In the incompressible elastic solid, the conservation of mass and momentum also require that

$$\nabla \cdot \mathbf{v}_s = 0, \tag{4}$$

$$\rho_s\left(\frac{\partial \mathbf{v}_s}{\partial t} + (\mathbf{v}_s \cdot \nabla)\mathbf{v}_s\right) = \nabla \cdot \boldsymbol{\sigma}_s, \tag{5}$$

where $\mathbf{v}_s$ is the solid velocity, ρ_s is the solid density, and $\boldsymbol{\sigma}_s$ is the total solid stress tensor. For an incompressible solid, the total stress $\boldsymbol{\sigma}_s$ can be decomposed into an isotropic pressure part and an extra stress part

$$\boldsymbol{\sigma}_s = -p_s\mathbf{I} + \boldsymbol{\tau}_s. \tag{6}$$

Instead of using the usual constitutive relation where the extra stress tensor $\boldsymbol{\tau}_s$ is proportional to the *Cauchy–Green* strain tensor (as a function of the gradient of the displacement field $\mathbf{u}_s$ with respect to the reference configuration), here we derive a new constitutive equation for $\boldsymbol{\tau}_s$. Starting from the displacement–velocity relationship

$$\frac{D\mathbf{u}_s}{Dt} = \mathbf{v}_s, \tag{7}$$

where D/Dt is a material derivative, an evolution equation for tensor $\mathbf{S}$ can be derived (see Appendix A)

$$\frac{\partial \mathbf{S}}{\partial t} + (\mathbf{v}_s \cdot \nabla)\mathbf{S} + \mathbf{S}(\nabla\mathbf{v}_s)^T + (\nabla\mathbf{v}_s)\mathbf{S} = \frac{1}{2}[\nabla\mathbf{v}_s + (\nabla\mathbf{v}_s)^T], \tag{8}$$

where $(\nabla v)_{ij} = \partial v_j/\partial x_i$ and $\mathbf{S}$ is the so called Eulerian *Almansi* strain tensor

$$\mathbf{S} = \frac{1}{2}[\nabla\mathbf{u}_s + (\nabla\mathbf{u}_s)^T - \nabla\mathbf{u}_s(\nabla\mathbf{u}_s)^T]. \tag{9}$$

We may next introduce a constitutive relation for a “Neo–Hookean” elastic material

$$\boldsymbol{\tau}_s = 2\eta_s\mathbf{S}, \tag{10}$$

where η_s is the shear modulus of the solid. Thus, the combination of Eqs. (8) and (10) leads to

$$\overset{\Delta}{\boldsymbol{\tau}}_s \equiv \frac{\partial \boldsymbol{\tau}_s}{\partial t} + (\mathbf{v}_s \cdot \nabla)\boldsymbol{\tau}_s + \boldsymbol{\tau}_s(\nabla\mathbf{v}_s)^T + (\nabla\mathbf{v}_s)\boldsymbol{\tau}_s = \eta_s[\nabla\mathbf{v}_s + (\nabla\mathbf{v}_s)^T], \tag{11}$$

where $\overset{\Delta}{\boldsymbol{\tau}}_s$ is the so-called lower-convected time derivative which is known to be objective [31,32]. Particularly, this derivative can be regarded as a rate of change following the material which takes into account the translational and rotational motion of the material, as well as the rate of deformation [33]. Eq. (11) serves as the constitutive equation for an elastic solid. In particular, it should be noted that the displacement field does not directly appear in this constitutive equation.

We may non-dimensionalize the governing equations by choosing the characteristic velocity scale $\dot{\gamma}d_p$, the length scale d_p, the time scale $\dot{\gamma}^{-1}$, the pressure and stress scale $\mu_f\dot{\gamma}$. Here we keep the same notation for the dimensionless variables as their dimensional counterparts. The governing equations (Eqs. (2), (3), (5) and (11)) are reduced to

$$Re\left(\frac{\partial \mathbf{v}_f}{\partial t} + \mathbf{v}_f \cdot \nabla \mathbf{v}_f\right) = -\nabla p_f + \nabla \cdot \boldsymbol{\tau}_f, \tag{12}$$

$$\boldsymbol{\tau}_f = \nabla \mathbf{v}_f + (\nabla \mathbf{v}_f)^T, \tag{13}$$

$$Re\left(\frac{\partial \mathbf{v}_s}{\partial t} + \mathbf{v}_s \cdot \nabla \mathbf{v}_s\right) = -\nabla p_s + \nabla \cdot \boldsymbol{\tau}_s, \tag{14}$$

$$Ca\left(\frac{\partial \boldsymbol{\tau}_s}{\partial t} + (\mathbf{v}_s \cdot \nabla)\boldsymbol{\tau}_s + \boldsymbol{\tau}_s(\nabla \mathbf{v}_s)^T + (\nabla \mathbf{v}_s)\boldsymbol{\tau}_s\right) = \nabla \mathbf{v}_s + (\nabla \mathbf{v}_s)^T, \tag{15}$$

where $Re = \rho\dot{\gamma}d_p^2/\mu_f$ is the Reynolds number, and $Ca = \mu_f\dot{\gamma}/\eta_s$ is the Capillary number which represents the ratio of the viscous force in the fluid and the elastic force in the solid. It should be pointed out that this definition of Ca is different from that of fluid vesicles because here η_s is the bulk shear modulus (with a unit N/m^2) instead of the membrane shear modulus (with a unit N/m) used in vesicles. Since the particles are neutrally buoyant, the densities of the solid and fluid are the same, $\rho_f = \rho_s = \rho$. The dimensionless continuity equations for the fluid and solid have the same form as Eqs. (1) and (4), respectively.

At the fluid–solid interface, coupling conditions are required for the solutions in the two phases. The velocity should satisfy the no-slip condition

$$\mathbf{v}_f = \mathbf{v}_s. \tag{16}$$

The traction force is required to be continuous across the interface

$$\boldsymbol{\sigma}_f \cdot \mathbf{n} = \boldsymbol{\sigma}_s \cdot \mathbf{n}, \tag{17}$$

where $\mathbf{n}$ is the unit normal vector at the interface.

On the moving walls, no-slip boundary condition is also applied. And at the two ends in the x-direction as shown in Fig. 1, the periodic boundary condition is used.

The governing equations (Eqs. (1), (4), (12), (13), (14) and (15)) coupling with the interfacial conditions (Eqs. 16 and 17) complete the mathematical description for our physical problem. The unknown variables in both the fluid and the solid phases are the velocity, pressure and stress, which can be solved simultaneously by an ALE finite element method (FEM). In the ALE method, the mesh is allowed to move with a given mesh velocity

$$\mathbf{v}_m = \left.\frac{\partial \mathbf{x}(\xi, t)}{\partial t}\right|_{\xi}, \tag{18}$$

where ξ is a referential mesh point and $\mathbf{x}$ is its physical coordinate. This mesh velocity does not necessarily follow the material movement [13]. It is convenient to design an appropriate mesh movement strategy to track the moving object accurately without degrading the mesh quality. The mesh velocity may be obtained by solving an elliptic equation

$$\nabla \cdot (k^e \nabla \mathbf{v}_m) = 0, \tag{19}$$

where k^e is the inverse of the local element volume [3]. The mesh velocity may be set to be zero at the moving solid walls. At the fluid–solid interface, the mesh velocity is required to follow the interface, however, is also allowed to slip along the tangential direction, which corresponds to

$$(\mathbf{v}_m - \overline{\mathbf{V}}_s) \cdot \mathbf{n} = (\mathbf{v}_s - \overline{\mathbf{V}}_s) \cdot \mathbf{n}, \tag{20}$$

$$(\mathbf{v}_m - \overline{\mathbf{V}}_s) \cdot \mathbf{t} = 0, \tag{21}$$

where $\overline{\boldsymbol{V}}_{\boldsymbol{s}}$ is an average velocity of the moving particle (a fixed vector for a given particle at a certain time instant), $\mathbf{n}$ and $\mathbf{t}$ are the unit normal and tangential vectors of the interface.

In the moving mesh frame, the variables are defined based on the referential mesh ξ, leading to a different evaluation for the material derivative

$$\frac{D}{Dt} = \frac{\partial}{\partial t} + \mathbf{v} \cdot \nabla = \left.\frac{\partial}{\partial t}\right|_{\xi} + (\mathbf{v} - \mathbf{v}_m) \cdot \nabla. \tag{22}$$

Denote $\Omega(t)$ as the computational domain at a given instant $t \in [0, T]$, which contains the fluid domain $\Omega_f(t)$, the solid domain $\Omega_s(t)$. The boundaries of the fluid and solid domain are $\partial\Omega_f(t)$ and $\partial\Omega_s(t)$, respectively. Therefore, we can discretize the governing equations following the standard Galerkin formulation [1,3]

$$\int_{\Omega} \left\{ Re\frac{D\mathbf{v}}{Dt} \cdot \tilde{\mathbf{v}} - p\nabla \cdot \tilde{\mathbf{v}} + \boldsymbol{\tau} : \nabla\tilde{\mathbf{v}} \right\} d\Omega = 0, \tag{23}$$

$$\int_{\Omega} -(\nabla \cdot \mathbf{v})\tilde{p}\, d\Omega = 0, \tag{24}$$

$$\int_{\Omega_f} \{\boldsymbol{\tau}_f - (\nabla \mathbf{v}_f + (\nabla \mathbf{v}_f)^T)\} : \tilde{\boldsymbol{\tau}}\, d\Omega = 0, \tag{25}$$

$$\int_{\Omega_s} \left\{ Ca\left(\frac{D\boldsymbol{\tau}_s}{Dt} + \boldsymbol{\tau}_s(\nabla \mathbf{v}_s)^T + (\nabla \mathbf{v}_s)\boldsymbol{\tau}_s\right) - (\nabla \mathbf{v}_s + (\nabla \mathbf{v}_s)^T) \right\} : \tilde{\boldsymbol{\tau}}\, d\Omega = 0, \tag{26}$$

where $\tilde{\mathbf{v}}$, $\tilde{p}$ and $\tilde{\tau}$ are test functions. In our implementation, a mixed finite element is used, where different interpolation functions are chosen for different unknown variables, which satisfies the LBB condition [3]. The discrete solution for the fluid velocity is approximated by piecewise quadratic functions which is continuous all over the domain (P2). However, The solutions of the pressure and stress are assumed to be continuous only in either fluid (Ω_f) or solid domain (Ω_s). At the fluid–solid interface $\partial\Omega_s$, only the traction force is required to be continuous (Eq. (17)). Thus, discontinuities are allowed for the pressure and stress components across the interface. Within either Ω_f or Ω_s, the discrete solution for the pressure is piecewise linear (P1) and the discrete solution for the stress is piecewise quadratic (P2). For this type of mixed finite elements, it is known that when Re is small, the numerical solution of the flow field can achieve 3rd order accuracy in space [34]. For this study, the temporal descretization implemented in the solver is a 2nd order finite difference scheme.

The governing equations for both the fluid and solid phases can be reduced to a similar nonlinear system of algebraic equations which is solved by a modified Newtonian–Raphson algorithm [3]. Specifically, in each non-linear iteration, a linear system

$$\begin{pmatrix} T_1 & T_2 & 0 \\ U_1 & U_2 & P \\ 0 & P^T & 0 \end{pmatrix} \begin{pmatrix} \tau \\ \mathbf{v} \\ p \end{pmatrix} = \begin{pmatrix} \mathrm{Res}_\tau \\ \mathrm{Res}_\mathrm{u} \\ \mathrm{Res}_\mathrm{p} \end{pmatrix}$$

is solved by a generalized minimal residual (GMRES) method [35], where all submatrices are sparse. An incomplete LU (ILU) preconditioner [36] is used to accelerate the convergence.

3. Numerical results and analysis

Initially, the flow field and the particle are assumed to be at rest. The particle is circular in the unstressed state. The bounding walls of the channel are set to a given velocity to start the simulation. When the shear flow is developed inside the channel, the particle experiences transient deformation where elastic waves can be observed propagating inside the solid. The particle then gradually reaches an equilibrium elliptic shape. The dynamics of the particle deformation is governed by the coupling of the elasticity of the Neo–Hookean material with the hydrodynamics of the bulk viscous fluid. As seen from Eqs. (12)–(15), two dimensionless numbers Re and Ca completely describe the flow around and deformation inside the solid particle.

For our problem, the size of the channel is assumed to be large enough with respective to the particle size so that the particle deformation is unaffected by the outer boundaries. To examine the influences of the outer boundaries on the results, we computed cases for H/d_p changing from 4 to 16, and found that when $H/d_p > 6$, the computed equilibrium shape of the particle does not have any noticeable difference. Therefore, we choose $H/d_p = 8$ for the computed cases shown in this section.

3.1. Validation of computational codes

Fig. 2(a) shows the equilibrium particle shape at $Re = 0.5$ and $Ca = 0.2$. The arrows represent velocities of material elements at the particle surface. Obviously, after the equilibrium shape is achieved, the material inside the particle experiences a tank-treading motion, which is similar to the motion of fluid vesicles enclosed by incompressible membrane in viscous shear flow. As shown in Fig. 2(b), equilibrium shapes of the particle are compared by using different mesh sizes and time steps. "○" represents the result on a coarse mesh with 100 nodes along the particle surface, while "+" the result on a refined mesh with 150 nodes. The time step for the coarse mesh is $\Delta t = 0.001$ s and the refined mesh $\Delta t = 0.0005$ s. The comparison

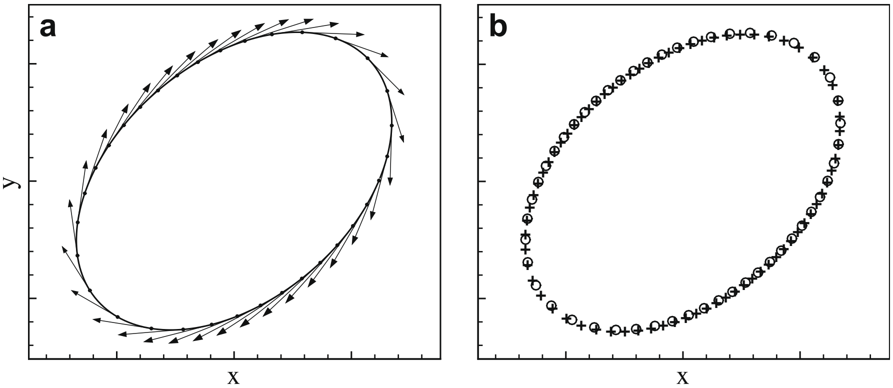

Fig. 2. Elastic particle deforms in a viscous shear flow at $Re = 0.5$ and $Ca = 0.2$. (a) Equilibrium particle shape. The velocities of the material elements at the particle surface are shown as the arrows. (b) Mesh resolution test. "○" represents result on a coarse mesh; "+" represents the result on a refined mesh.

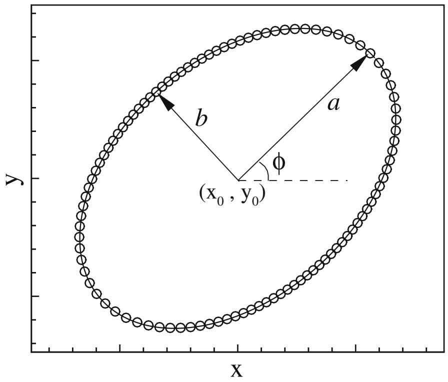

Fig. 3. Fitting of a computed equilibrium particle shape, shown in Fig. 2, into an ellipse. "∘" represents the computed result and the solid line represents the fitted ellipse.

indicates that the particle shape is independent of mesh size and time step; thus the solution has converged. However, when dealing with larger deformations with higher values of *Ca*, the particle will be more elongated with sharper tips. The refined mesh with 150 nodes along the particle surface and small time step ($\Delta t \leqslant 0.0005$ s) are employed for the simulations presented in this section. The number of the elements used in this simulation is about 12,000, and the total number of unknowns is about 125,000.

The equilibrium shape of the deformed particle can be fit into a standard ellipse

$$\frac{[(x-x_0)\cos\phi+(y-y_0)\sin\phi]^2}{a^2}+\frac{[-(x-x_0)\sin\phi+(y-y_0)\cos\phi]^2}{b^2}=1,$$

where (x_0, y_0) is the center of the ellipse, ϕ is its orientation, a and b are the semimajor and semiminor axis, respectively. As shown in Fig. 3, the particle shape fits perfectly into a standard ellipse when *Ca* is small.

After the particle deforms into the equilibrium shape, we stop the flow by setting the wall velocity $U = 0$. The flow field decays rapidly. Due to the elasticity of the Neo–Hookean material, the deformed particle gradually recovers its unstressed circular shape as the fluid viscous stress applied at the particle surface dies down. This transitional process is shown in Fig. 4(a–f) at six consecutive time instants. It is observed that the particle has already reached its equilibrium shape at $t = 1.0$ s. After stopping the moving wall at $t = 4.0$ s, the particle quickly recovers initial circular shape. The recovered circular shape in Fig. 4(f) is identical to its initial unstressed shape.

3.2. Elastic waves in transient deformation

When the shear flow field is being developed in the channel, the particle first experiences a transient deformation when the particle is stretched and elongated, similar to Fig. 4(a) and (b). During the transient deformation, it is observed that symmetric elastic waves propagate inside the particle with a certain characteristic wave speed. For linear elastic material, it is well-known that the elastic waves travel at a speed determined by $c_s = \sqrt{\eta_s/\rho_s}$ [37]. For the computed case, we choose $\eta_s = 500$ Pa and $\rho_s = 1.0\ \mathrm{g/cm^3}$. Therefore, the characteristic wave speed is $c_s = 22.4$ cm/s.

To show these elastic waves, we monitor flow variables at certain fixed points inside the particle during its deformation. Fig. 5(a) shows the variation of v velocity component with time at a sampling point close to the particle center. The velocity fluctuation indicates a dominant frequency. A spectrum analysis is performed in Fig. 5(b) where the dominant frequency is found to be $f_0 = 53.8$ Hz, which corresponds to a wave period $T_0 = 1/f_0 = 0.0186$ s. During the sampling time (from $t = 0.1$ s to $t = 0.2$ s), it is reasonable to choose the characteristic wave length as the shorter diameter of the deformed particle $L_0 = 2\bar{b} \approx 0.420$ cm. Therefore, we can estimate the characteristic wave speed as $c_s^* = L_0/T_0 = 22.6$ cm/s, which agrees very well with the theoretical value of c_s mentioned above.

To better visualize the elastic waves in the particle, we plot the isolines of the v velocity component in Fig. 6(a–f) during approximately one wave period as marked in Fig. 5(a) from $t = 0.135$ s to $t = 0.153$ s, which clearly show a symmetric wave is propagating inside the particle.

In computation, the elastic wave propagation has to be accurately captured to resolve the transient deformation of the particle. As a result, we have to select time steps to be much smaller than the characteristic wave period T_0.

3.3. Equilibrium shape as a function of the Capillary number

Next, we investigate the effects of *Ca* on the equilibrium particle shapes in the Stokes flow regime. In the limit of small *Re*, it can be seen from Eqs. (12)–(15) that *Ca* will be the only dimensionless number which characterizes the elastic deformation.

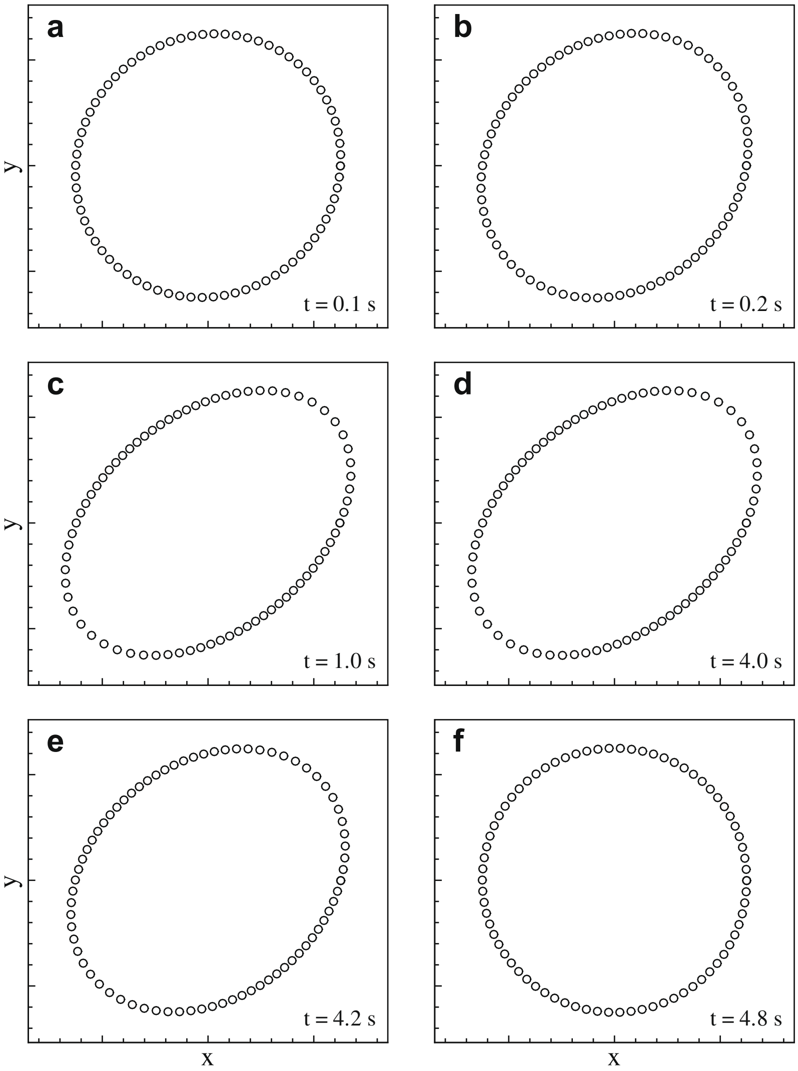

Fig. 4. Deformation and recovery of a circular particle in a shear flow at $Re = 0.125$ and $Ca = 0.2$.

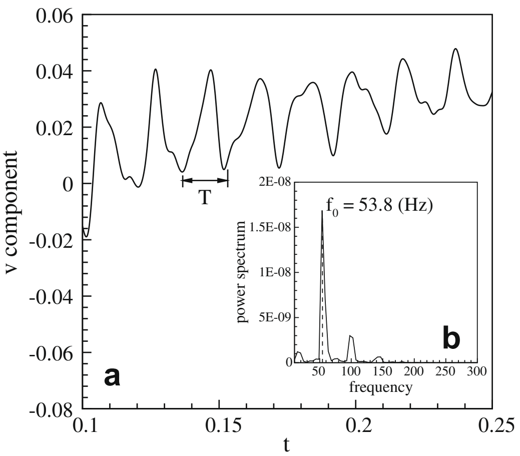

Fig. 5. Spectrum analysis of the velocity component as a function of time at a point inside the particle. (a) The variation of v velocity component with time. (b) The power spectrum of this velocity variation.

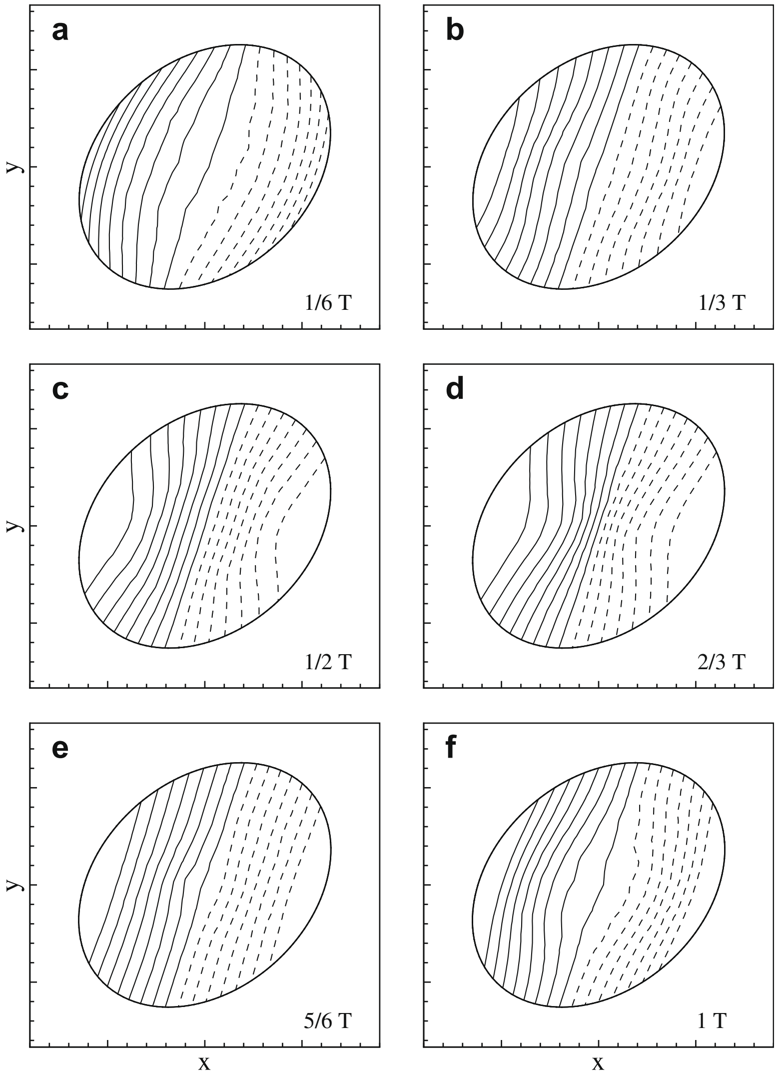

Fig. 6. The isolines for the v velocity component inside the particle during one period of the elastic wave propagation from $t = 0.135$ s to $t = 0.153$ s as marked in Fig. 5(a). The solid lines represent positive values while dashed lines represent negative values.

Fig. 7 compares the equilibrium shapes of the particle at three different values of Re ($Re = 0.05, 0.125$, and 0.5), when $Ca = 0.2$. It is observed that the shapes at $Re = 0.125$ and $Re = 0.05$ are not distinguishable, while the shape at $Re = 0.5$ is slightly different from the other two cases. Thus, we confirm that $Re = 0.125$ is small enough for effects of Re to be negligible.

Fig. 8(a–d) show the equilibrium particle shapes at $Ca = 0.02, 0.08, 0.2, 0.5$. In our computation, the fluid viscosity μ_f and the shear rate $\dot{\gamma}$ are fixed. Thus, small Ca corresponds to large shear modulus η_s, which means the material is stiff, and vice versa. In Fig. 8(a), the deformation is very small. The particle is similar to a rigid body. Fig. 8(d) indicates that the deformed particle still fits into an ellipse even at very large deformation. The deformation can be quantified by a dimensionless parameter

$$D = \frac{a - b}{a + b}, \tag{27}$$

which is commonly used to characterize the deformation of fluid vesicles[22,26] and droplets [5,38,39]. The computed variation of the deformation parameter with the Capillary number Ca is shown in Fig. 9(a). From the figure, it is clear that there is a linear regime where $D = Ca$ when $Ca < 0.3$. The orientation of the deformed particle is shown in Fig. 9(b). A similarly linear relationship for this orientation as a function of Ca is observed. It is expected that when Ca tends to zero, the maximum orientation approaches 45°. During its deformation, it is found that the transient shapes of the particle can be fitted into a series of ellipses. Therefore, we can track the temporal evolution of the deformation parameter D, as shown in Fig. 10. It is observed that D reaches its equilibrium value monotonically.

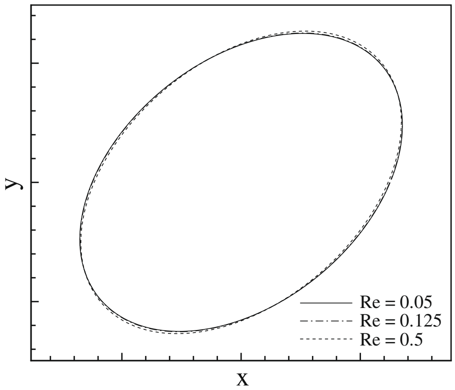

Fig. 7. Equilibrium particle shapes at $Re = 0.05, 0.125$ and 0.5. $Ca = 0.2$ is fixed.

To check the total mass conservation in the deformed particle, we evaluated the relative change of the particle volume (area in 2D), $1 - A/A_0 = 1 - 4ab/d_p^2$, which is plotted in Fig. 11 at different values of Ca. A/A_0 is the ratio of the area of the ellipse to that of the initial circle. In general, the area of the particle is well conserved within numerical error, although a jump (still within 0.5%) is observed at $Ca = 0.65$. At large deformations, such a large error does not necessarily imply that the mass of the particle is not as well conserved, since the actual shape of the deformed particle starts to deviate from the standard ellipse.

3.4. Perturbation analysis in the limit of small Capillary number

In the Stokes flow regime, it is possible to carry out a perturbation analysis in terms of small parameter Ca to get the analytical solution to the flow field and the particle deformation. At the leading order ($O(1)$), the particle is circular and expe-

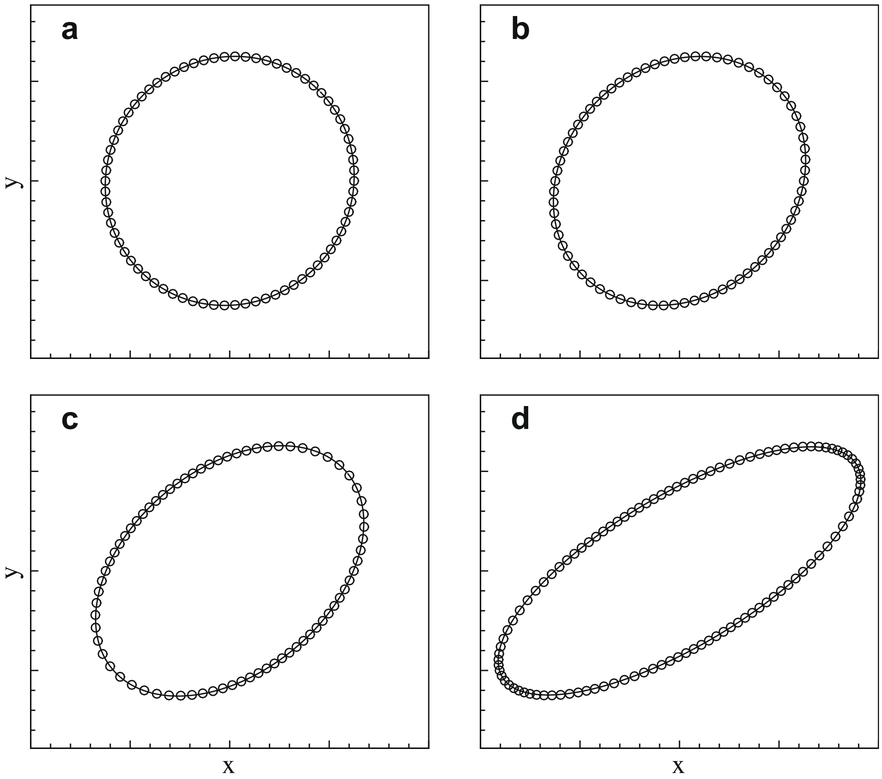

Fig. 8. Equilibrium particle shapes at $Re = 0.125$: (a) Ca=0.02; (b) Ca=0.08; (c) Ca=0.2; (d) Ca=0.5. "○" represents computed results, and the solid line represents fitted ellipses.

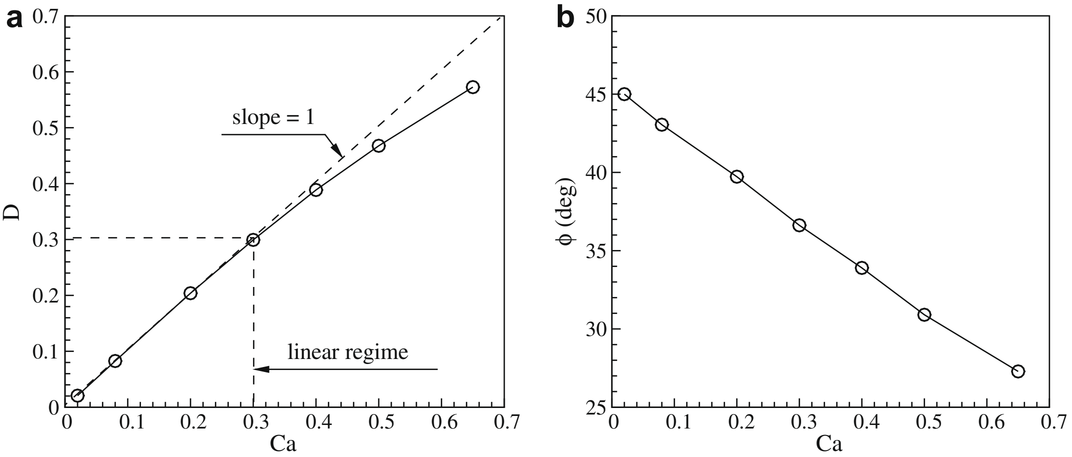

Fig. 9. (a) Deformation parameter D as a function of Ca; (b) orientation ϕ as a function of Ca.

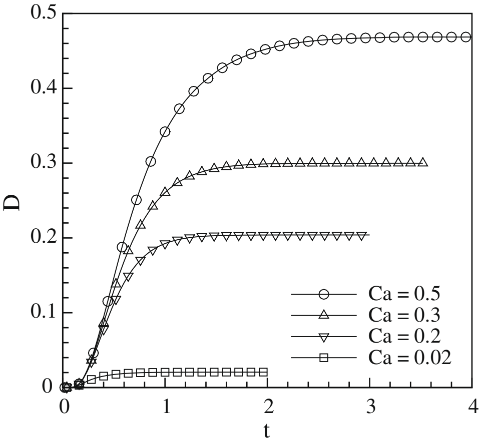

Fig. 10. The evolution of the deformation parameter D as a function of time for $Ca = 0.02$, 0.2, 0.3 and 0.5. t is the nondimensional time (scaled by $\dot{\gamma}^{-1}$).

Fig. 11. Relative change of area of the deformed particle as a function of Ca.

riences a rigid body rotation. Fig. 12 shows a 2D circular cylinder rotating clockwise in the viscous shear flow with angular velocity ω. Bretherton [40] obtained the Stokes flow solution for this rotating cylinder. The dimensionless stream function ψ is given by

$$\psi(r,\theta)=\frac{1}{2}r^2\sin^2\theta-\frac{1}{4}\left[2(1-2\omega)\ln r+1+\left(\frac{1}{r^2}-2\right)\cos 2\theta\right]. \tag{28}$$

The dimensionless velocity field is

$$v_r=\frac{1}{r}\frac{\partial\psi}{\partial\theta}=\frac{1}{2r}\left(r-\frac{1}{r}\right)^2\sin 2\theta, \tag{29}$$

$$v_\theta=-\frac{\partial\psi}{\partial r}=\frac{1}{2}\left(\frac{1-2\omega}{r}-r\right)+\frac{1}{2r}\left(r^2-\frac{1}{r^2}\right)\cos\theta. \tag{30}$$

Here we neglect the subscript "*f*" for solutions in the fluid. For a freely rotating cylinder, it is shown that $\omega=-1/2$ to guarantee zero net torque [40]. With $\omega=-1/2$, the pressure field is given as

$$p(r,\theta)=p_\infty-\frac{2}{r^2}\sin 2\theta. \tag{31}$$

At the particle surface ($r=1$), the stress distribution can be evaluated as

$$\sigma_{rr}=\sigma_{\theta\theta}=-p_\infty+2\sin 2\theta, \tag{32}$$

$$\sigma_{r\theta}=2\cos 2\theta. \tag{33}$$

To derive the induced deformation due to this stress distribution at the particle surface, the solutions in the solid can be expanded in the powers of *Ca*

$$\mathbf{v}=\mathbf{v}^0+Ca\times\mathbf{v}^1+O(Ca^2), \tag{34}$$

$$\boldsymbol{\tau}=\boldsymbol{\tau}^0+Ca\times\boldsymbol{\tau}^1+O(Ca^2), \tag{35}$$

$$p=p^0+Ca\times p^1+O(Ca^2). \tag{36}$$

The subscript "*s*" for solutions in the solid is also neglected for convenience.

At the 0*th* order ($O(1)$), we have

$$\mathbf{v}^0=-\frac{1}{2}r\mathbf{e}_\theta, \tag{37}$$

$$-\nabla p^0+\nabla\cdot\boldsymbol{\tau}^0=0, \tag{38}$$

and 0*th* order extra stress tensor $\boldsymbol{\tau}^0$ has to be determined by the constitutive equation at the 1*st* order,

$$\overset{\Delta}{\boldsymbol{\tau}}{}^0=\nabla\mathbf{v}^1+(\nabla\mathbf{v}^1)^T. \tag{39}$$

As an alternative way to resolve $\boldsymbol{\tau}^0$ by the perturbation analysis, we perform a numerical computation at a small *Ca* to obtain the information for $\mathbf{v}^1$. At $Re=0.125$ and $Ca=0.004$, Fig. 13(a) and (b) plot the isolines for the u and v velocity component, respectively. Inside the particle, as expected at the leading order, the u velocity component is proportional to y, while the v velocity component is proportional $-x$, which indicates a perfect rigid body rotation. Next, we examine the velocity profile

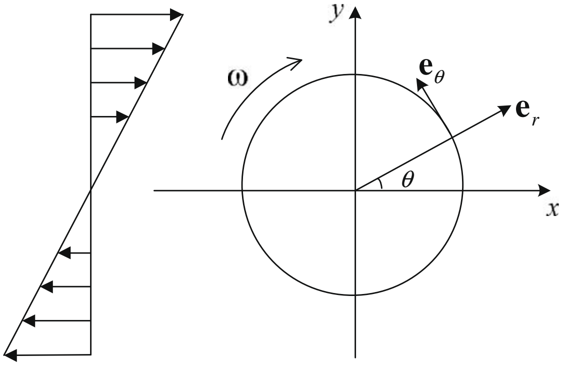

Fig. 12. Schematic of a 2D rotating cylinder in Stokes shear flow.

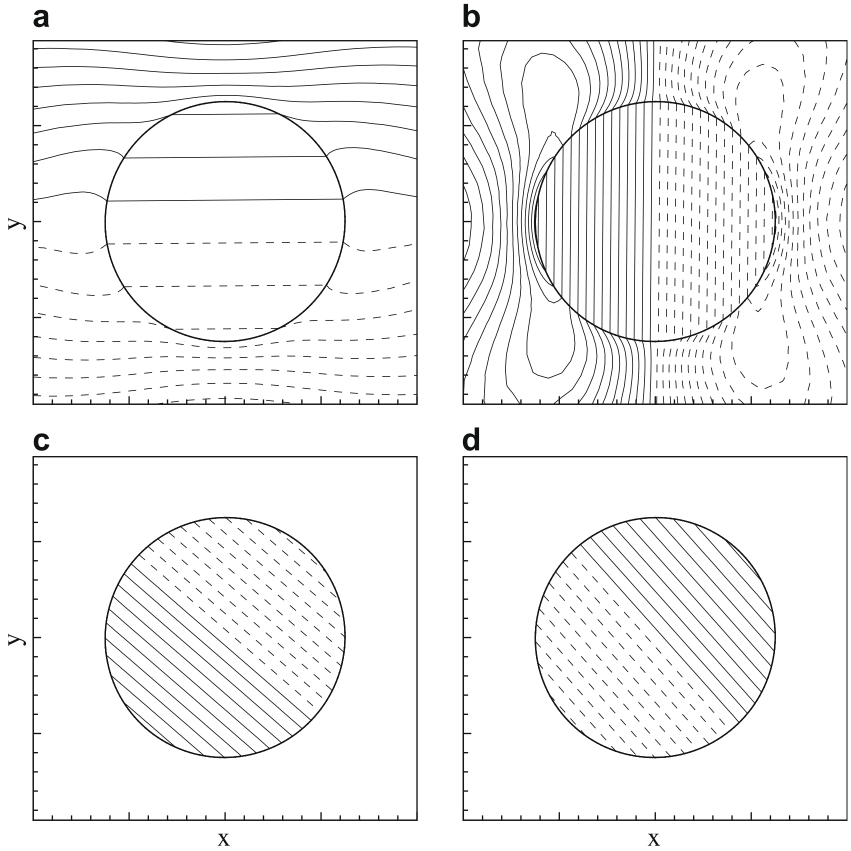

Fig. 13. Isolines for velocity components at $Re = 0.125$ and $Ca = 0.004$: (a) u velocity; (b) v velocity; (c) $u - y/2 \approx u^1$; (d) $v + x/2 \approx v^1$. The 1*st* order solution $\mathbf{v}^1$ is only plotted inside the particle. The solid lines represent positive values and dashed lines represent negative values.

inside the particle excluding this rigid body rotation. Fig. 13(c) and (d) plot the velocity deviation from the rigid body rotation. According to the perturbation expansion, this deviation should be dominated by the 1*st* order velocity solution $\mathbf{v}^1$. From the plots in Fig. 13(c) and (d), it is clearly observed that inside the particle, both u^1 and v^1 components are linear in x and y. Therefore, it is reasonable to assume that $\mathbf{v}^1$ take the form

$$\mathbf{v}^1 = (c_1 x + c_2 y)\mathbf{e}_x + (c_3 x - c_1 y)\mathbf{e}_y, \tag{40}$$

where c_i are unknown constants to be determined, and Eq. (40) satisfies the continuity equation. Physically, inside the solid particle it is expected that in addition to the rigid body rotation, a secondary motion corresponding to the velocity field given by Eq. (40) needs to be established to generate a stress field at the 0*th* order to balance the viscous force applied by the bulk fluid at the particle surface.

In the cylindrical coordinates, the velocity profile in Eq. (40) can be written as

$$\mathbf{v}^1 = r\left[c_1 \cos 2\theta + \left(\frac{c_2 + c_3}{2}\right)\sin 2\theta\right]\mathbf{e}_r + r\left[\left(\frac{c_3 - c_2}{2}\right) - c_1 \sin 2\theta + \left(\frac{c_2 + c_3}{2}\right)\cos 2\theta\right]\mathbf{e}_\theta. \tag{41}$$

The 0*th* order steady state solutions for the stress components and the pressure are derived in Appendix B. The components of the total stress tensor are found to be

$$\sigma^0_{rr} = -G(r) + A(r) - 2c_1 \sin 2\theta + (c_2 + c_3)\cos 2\theta, \tag{42}$$

$$\sigma^0_{\theta\theta} = -G(r) - A(r) + 2c_1 \sin 2\theta - (c_2 + c_3)\cos 2\theta, \tag{43}$$

$$\sigma^0_{r\theta} = -2c_1 \cos 2\theta - (c_2 + c_3)\sin 2\theta, \tag{44}$$

where $A(r)$ and $G(r)$ are related functions of the radial position only.

At the fluid–solid interface, it is required that $\boldsymbol{\sigma}^0_f \cdot \mathbf{n} = \boldsymbol{\sigma}^0_s \cdot \mathbf{n}$. Matching the solutions in Eqs. (42)–(44) evaluated at the particle surface with Eqs. (32) and (33), we have

$$c_1 = -1, c_3 = -c_2, -G(1) + A(1) = -p_\infty. \tag{45}$$

With velocity solutions at both 0*th* and 1*st* order in the solid, we can solve the pathline of a material element by using $\mathbf{v} = (dr/dt)\mathbf{e}_r + (rd\theta/dt)\mathbf{e}_\theta$. Substituting Eq. (45) into Eq. (41) and then combining the 0*th* order solution in Eq. (37), we can get

$$\frac{dr}{dt} = -Ca(\cos 2\theta)r + O(Ca^2), \tag{46}$$

$$\frac{d\theta}{dt} = -\frac{1}{2} + Ca(\sin 2\theta - c_2) + O(Ca^2). \tag{47}$$

Eqs. (46) and (47) can be combined to eliminate the time, and the resultant equation is integrated to obtain the pathline of a material element inside the particle

$$r^2\left(\frac{1}{2} + c_2 Ca - Ca\sin 2\theta\right) + O(Ca^2) = Constant. \tag{48}$$

Eq. (48) represents the trajectory of an ellipse with the semimajor and semiminor axis given by

$$a = r_{\min} = \sqrt{\frac{2A_0}{1 + 2Ca(c_2 + 1)}} = \sqrt{2A_0}(1 - Ca - c_2 Ca) + O(Ca^2),$$

$$b = r_{\max} = \sqrt{\frac{2A_0}{1 + 2Ca(c_2 - 1)}} = \sqrt{2A_0}(1 + Ca - c_2 Ca) + O(Ca^2),$$

where A_0 is a constant in Eq. (48) associated with a particular material element at the particle surface. The deformation parameter D is then evaluated by

$$D = \frac{2\sqrt{2A_0}Ca + O(Ca^2)}{2\sqrt{2A_0}(1 - c_2 Ca) + O(Ca^2)} = Ca + O(Ca^2). \tag{49}$$

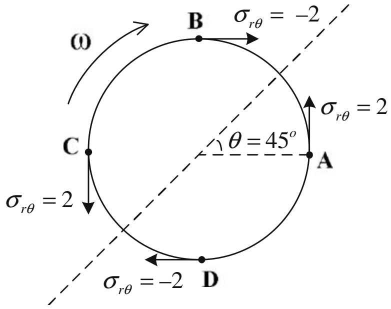

Fig. 14. An illustration of fluid force applied at different points on the particle surface: A ($\theta = 0^\circ$), B ($\theta = 90^\circ$), C ($\theta = 180^\circ$) and D ($\theta = 270^\circ$). The particle deforms symmetrically along the dashed line with an orientation of $\theta = 45^\circ$.

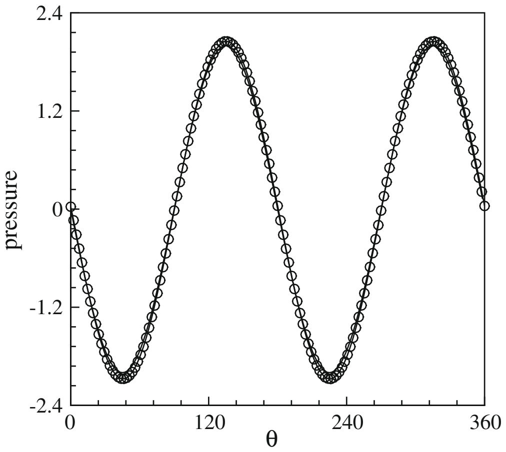

Fig. 15. Pressure distribution along the particle surface. "○" represents computational results; The solid line represents the Stokes solution (Eq. (31)) at $r = 1$.

Table 1
Comparison of the numerical results and perturbation solutions.

	Perturbation	Numerical
$\tau_{xx} + \tau_{yy}$	0.0	−0.01
τ_{xy}	2.0	2.08
ϕ	45°	44.98°

At the leading order, $D = Ca$, which is exactly observed numerically in Fig. 9(a). It is also noticed that the unknown constant c_2 does not affect the particle shape at the leading order. Additionally, when r reaches $r_{\max}$, $\sin 2\theta = 1$ which corresponds to the orientation angle of 45°. Numerical data shown in Fig. 9(b) at the limit of small Ca agrees with this theoretical observation. In Fig. 14, applied fluid forces $\boldsymbol{\sigma}_f \cdot \mathbf{n}$ are plotted at four points (A, B, C, D) along the particle surface, corresponding to $\theta = 0^\circ, 90^\circ, 180^\circ, 270^\circ$, respectively. Here the constant pressure p_∞ is neglected because it does not contribute to the particle deformation. Under the action of such a force distribution, the particle tends to deform symmetrically along the dashed line indicated in Fig. 14. The deformed particle will have an orientation at 45°.

We can also examine the pressure and the stress field at $Re = 0.125$ and $Ca = 0.004$. Fig. 15 indicates that the numerical solution for the pressure distribution along the particle surface agrees with the Stokes solution (Eq. (31)) with $p_\infty = 0$. Furthermore, the extra stress $\boldsymbol{\tau}^0$ at the boundary can be transformed to Cartesian coordinate

$$\boldsymbol{\tau}^0 = A(1)\cos 2\theta(\mathbf{e}_x\mathbf{e}_x - \mathbf{e}_y\mathbf{e}_y) + (2 + A(1)\sin 2\theta)(\mathbf{e}_x\mathbf{e}_y + \mathbf{e}_y\mathbf{e}_x). \tag{50}$$

Although $A(1)$ is still unknown, the value of $\tau_{xx} + \tau_{yy}$ should be zero and the mean value of τ_{xy} should be 2, which are all consistent with the numerical results listed in Table 1. The orientation of the deformed particle is computed as 44.98° which is in close agreement with the theoretical value.

3.5. *Particle–particle interactions in a shear flow*

In this section, we consider the interaction between two deformable particles in a shear flow at small Re. As shown in Fig. 16, two identical circular elastic particles (particle A and B) are initially placed symmetrically in the channel. The conditions for the simulation in this section correspond to $Re = 0.1$ and $Ca = 0.25$. The periodic boundary condition is applied in the x-direction, and the initial distance between the two particles ($2g_0$) is chosen as d_p.

Fig. 17 shows simulation results. In Fig. 17(a) and (b), after the shear flow has been developed, the circular particles quickly deform to an elliptic shape which is similar to the single particle situation. At the same time, the two particles move toward each other. During the translation, it is observed particle–particle interactions occur periodically with two interacting modes. At first, the two particles experience a "roll over" mode shown in Fig. 17(c) and (d). After the first two encounters, the interacting particles change to a "bounce back" mode as shown in Fig. 17(e) and (f). In this mode, the two particles move around separately in the left and right half of the channel. Eventually, both particles tend to their own equilibrium positions in the middle of the channel with an equal distance, consistent with the single particle situation presented earlier.

Different phases of the particle–particle interaction can be observed clearly by plotting the particle's y-position as functions of time, as shown in Fig. 18(a). At first, two particles come together quickly due to the initial deformation. Then as particles encounter each other whilst moving with the flow, they experience the "roll over" interacting mode (Fig. 17(c and d)) indicated as two peaks in Fig. 18(a) at around $t = 3$ s and $t = 10$ s. When $t > 20$ s, two particles move across the center line of

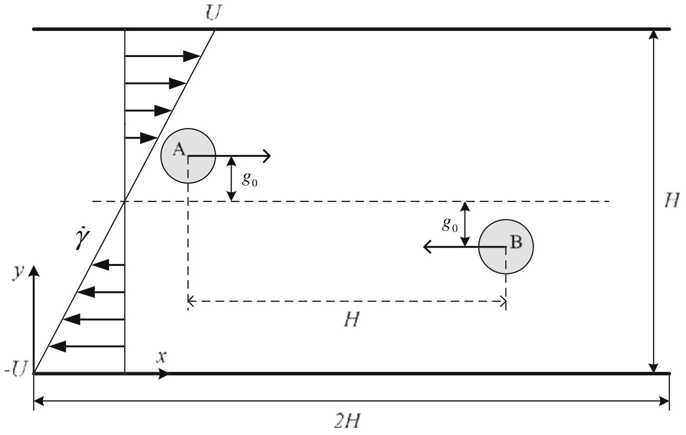

Fig. 16. Schematic for two elastic particles interacting in Stokes shear flow. The arrows at the particle centers represent the initial movements induced by the shear flow.

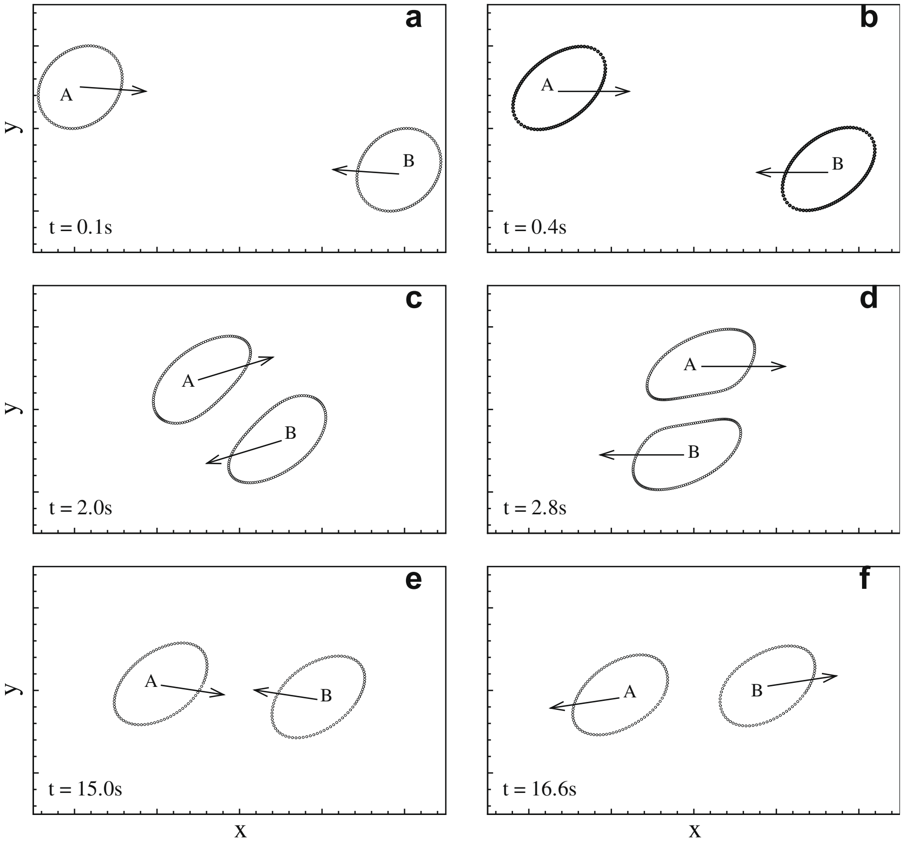

Fig. 17. Particle–particle interactions in a shear flow. (a) and (b): initial deformation; (c) and (d): "roll over" interacting mode; (e) and (f): "bounce back" interacting mode.

the channel periodically when they approach each other, which corresponds to a "bounce back" interacting mode (Fig. 17(e and f)). At later times ($t > 40$ s), the particle interaction is greatly weakened, and two particles tend to their corresponding equilibrium positions, which can also be visualized by plotting particle positions in the x-direction as a function of time in Fig. 18(b). The centers of the equilibrium particles are $(2, 2)$ for particle A, and $(6, 2)$ for particle B. Thus, particles finally settle down in the periodic channel with an equal distance of separation. The final equilibrium shape of the particles is plotted in Fig. 19. This shape exactly matches that from the single particle simulation under the same flow conditions. This comparison

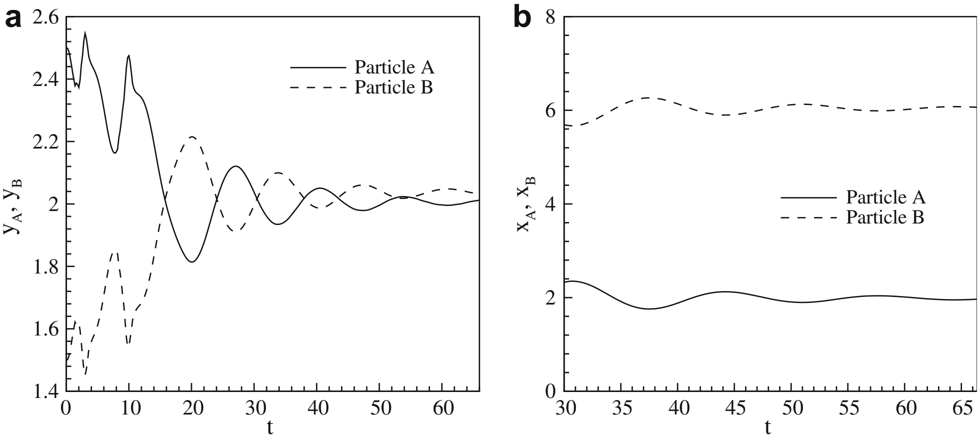

Fig. 18. (a) Variations of particle's y-position as functions of time. (b)Variations of particle's x-positions at later times when the particles settle into equilibrium.

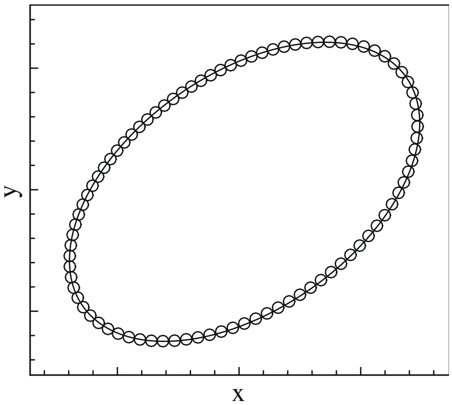

Fig. 19. Comparison of the equilibrium shapes of particles. "∘" represents the shape of particle A at $t = 60.0$ s. The solid line represents the equilibrium shape of the particle in the single particle simulation at the same conditions ($Re = 0.1$ and $Ca = 0.25$).

also indicates that the computational domain in the single particle simulations is long enough such that the dynamics of the particle deformation would not be affected if a longer channel length were to be used.

The mechanisms of hydrodynamic interactions can be explained by the pressure distribution in the flow field. As shown in Fig. 20(a and b), for the "roll over" mode, a high pressure area can be seen between the two particles. From this high pressure, there is a repulsive force keeping the particles apart. However, viscous forces applied by the bulk fluid can still overcome this repulsive force to push the particles into each other. In Fig. 20(c) and (d), however, a low pressure area is found in between the particles when particle A and B move close, which sucks them toward each other at first. When particles move across the center line of the channel, the applied shear forces change directions and gradually drag them apart.

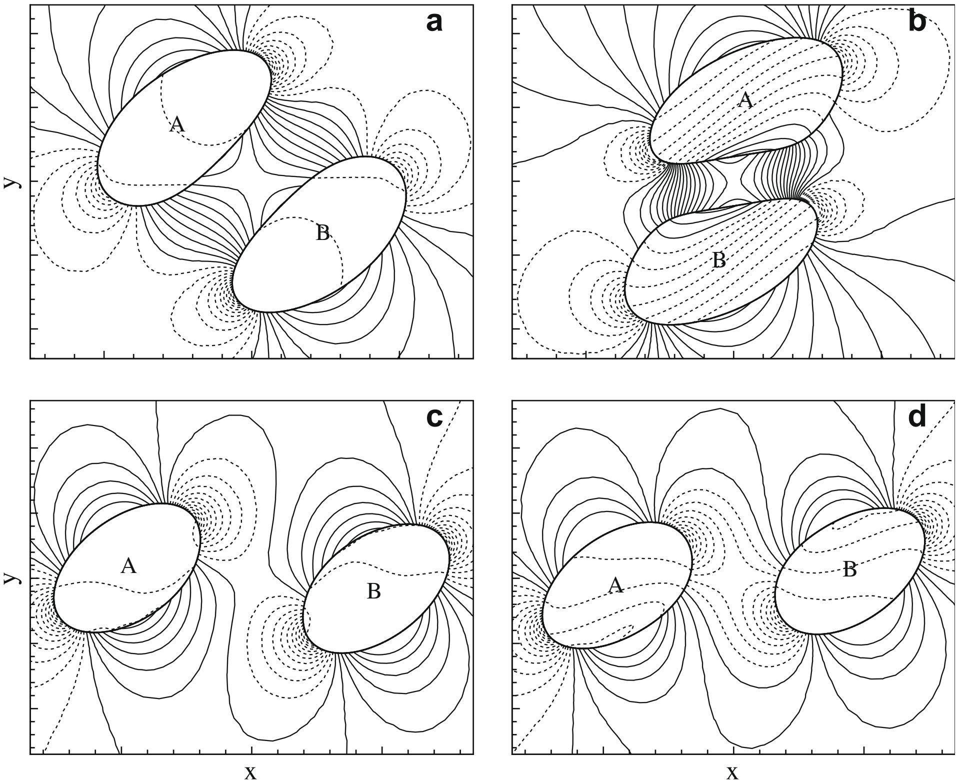

Fig. 20. Isolines of the pressure distribution at different times. (a) $t = 2.0$ s; (b) $t = 2.8$ s; (c) $t = 15.0$ s; (d) $t = 16.6$ s.

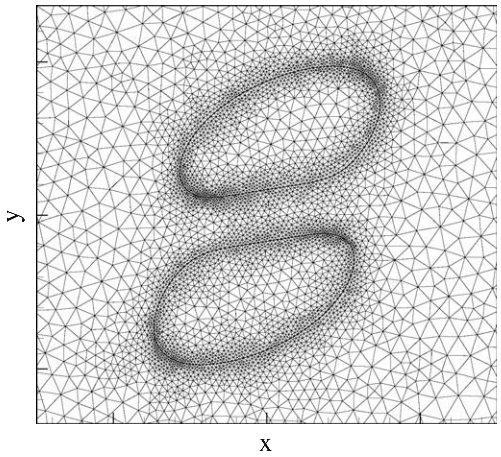

Fig. 21. The finite element mesh around two approaching particles corresponding to $t = 2.8$ *s* from Fig. 20(b).

As shown in Fig. 21 where two particles get close to each other at $t = 2.8$ s, the mesh generator in our solver is designed to refine the mesh adaptively in the region where particles are approaching each other [3]. There are always sufficiently fine elements in this region with the mesh size smaller than the minimum gap size between the approaching particles.

3.6. Effects of the Reynolds number on the equilibrium particle shape

So far, we have focused on situations at low *Re*. It is also interesting to investigate the effects of *Re* on the equilibrium particle shape. Fig. 22(a–d) shows equilibrium particle shapes at various Reynolds numbers with the Capillary number fixed at $Ca = 0.2$. We can observe that when $Re = 5$ (Fig. 22(a)), the equilibrium particle shape is slightly deviated from a standard

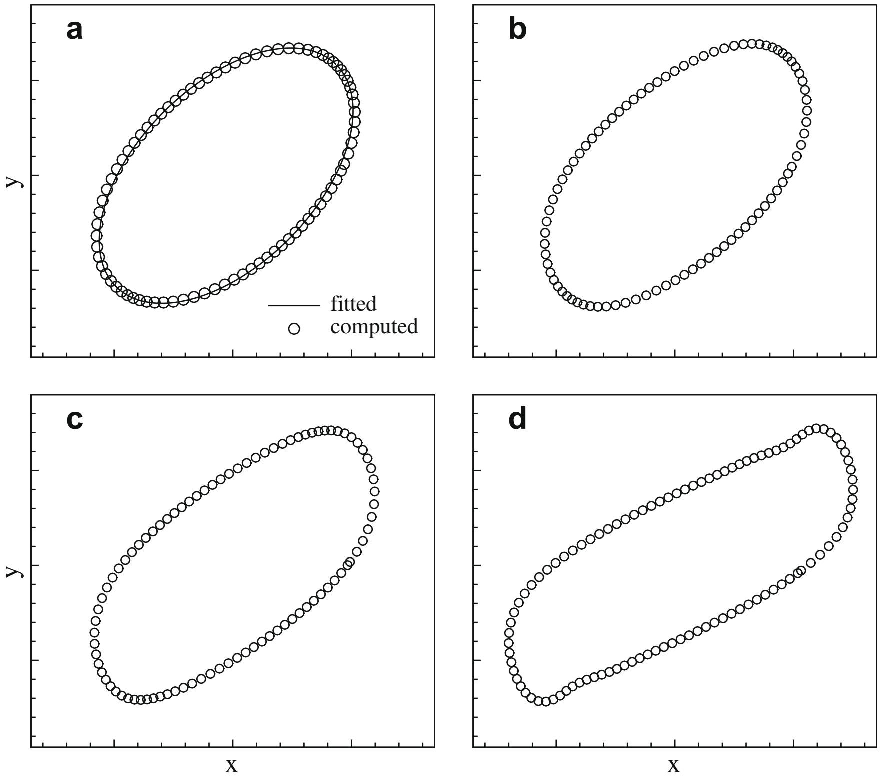

Fig. 22. Equilibrium particle shapes at $Ca = 0.2$: (a) Re = 5; (b) Re = 10; (c) Re = 20; (d) Re = 50.

ellipse. When *Re* is further increased to $Re = 10$ (Fig. 22b) and $Re = 20$ (Fig. (22)(c)), the particle becomes more elongated with two ends of large curvature pointing upwards and downwards. At $Re = 50$ (Fig. (22)(d)), horn-shaped corners appear at the particle ends. These shapes are very similar to the situations of liquid capsules with elastic membranes in a viscous shear flow at moderate *Re* [30]. It is expected that the coupling of *Re* and *Ca* would give rise to more complicated material behaviors of the suspension.

4. Conclusion

In this paper, we developed a new finite element technique to simulate 2D elastic particles deforming in viscous fluid flows. In the solid, an evolution equation for the Eulerian *Almansi* strain tensor is derived to describe the elastic deformation. A constitutive equation is thus established for an incompressible "Neo–Hookean" material. By using an ALE finite element formulation, we implemented a monolithic solver to solve both the fluid and the solid phase simultaneously. It is demonstrated that the new ALE finite element scheme is stable, accurate and robust for simulations of fluid–structure interactions.

Using the new ALE finite element scheme, we investigated deformations of elastic particles in a Newtonian viscous shear flow. It was found that

(1) In the Stokes flow regime, after the initial transient deformation, the particle eventually deforms into an equilibrium elliptic shape. The material points inside the particle experience a tank-treading like motion with a steady velocity field. For the deformed particle, the deformation parameter D has been characterized as a function of *Ca*. For $Ca < 0.3$, it is found that $D = Ca$, which agrees with theoretical results from a perturbation analysis in the limit of small *Ca*.
(2) It is observed that the elastic waves propagating inside the particle play an important role during its transient deformation. The speed of the elastic waves may be much faster than the flow velocity. Therefore, the time step used in the simulation has to be small enough to appropriately resolve these waves.
(3) In the simulation of two particles in a shear flow, complicated interactions between particles are observed. Two particles eventually settle into their corresponding equilibrium positions with an identical elliptic shape which exactly matches the deformed shape of the single particle under the same flow conditions.
(4) At moderate *Re*, the equilibrium particle shape can deviate significantly from a standard ellipse, which indicates complicated material behaviors induced by the coupling of *Re* and *Ca*.

Acknowledgment

The work is partially supported by the Nano/Bio Interface Center at the University of Pennsylvania through the NSF NSEC DMR-045780.

Appendix A. Evolution equation for the Eulerian *Almansi* strain tensor

The Cartesian index form of the displacement–velocity relationship, Eq. (7) or $D\mathbf{u}/Dt = \mathbf{v}$, reads

$$\frac{\partial u_i}{\partial t} + v_k \frac{\partial u_i}{\partial x_k} = v_i. \tag{A.1}$$

The gradient of Eq. (A.1) takes the form

$$\frac{\partial}{\partial t}\left(\frac{\partial u_i}{\partial x_j}\right) + v_k \frac{\partial}{\partial x_k}\left(\frac{\partial u_i}{\partial x_j}\right) + \left(\frac{\partial v_k}{\partial x_j}\right)\left(\frac{\partial u_i}{\partial x_k}\right) = \frac{\partial v_i}{\partial x_j}. \tag{A.2}$$

Adding the transpose of Eq. (A.2) to itself, we get

$$\frac{\partial}{\partial t}\left(\frac{\partial u_i}{\partial x_j} + \frac{\partial u_j}{\partial x_i}\right) + v_k \frac{\partial}{\partial x_k}\left(\frac{\partial u_i}{\partial x_j} + \frac{\partial u_j}{\partial x_i}\right) + \left(\frac{\partial v_k}{\partial x_j}\right)\left(\frac{\partial u_i}{\partial x_k}\right) + \left(\frac{\partial v_k}{\partial x_i}\right)\left(\frac{\partial u_j}{\partial x_k}\right) = \frac{\partial v_i}{\partial x_j} + \frac{\partial v_j}{\partial x_i}. \tag{A.3}$$

With the definition of the velocity in Eq. (A.1), it can be shown that

$$\frac{\partial v_k}{\partial x_j}\left(\frac{\partial u_k}{\partial x_i}\right) + \frac{\partial v_k}{\partial x_i}\left(\frac{\partial u_k}{\partial x_j}\right) = \frac{\partial}{\partial t}\left[\frac{\partial u_k}{\partial x_i}\frac{\partial u_k}{\partial x_j}\right] + v_l \frac{\partial}{\partial x_l}\left(\frac{\partial u_k}{\partial x_j}\frac{\partial u_k}{\partial x_i}\right) + \left[\left(\frac{\partial v_l}{\partial x_j}\right)\left(\frac{\partial u_k}{\partial x_l}\right)\left(\frac{\partial u_k}{\partial x_i}\right) + \left(\frac{\partial v_l}{\partial x_i}\right)\left(\frac{\partial u_k}{\partial x_l}\right)\left(\frac{\partial u_k}{\partial x_j}\right)\right]. \tag{A.4}$$

Adding Eq. (A.4) to Eq. (A.3) and rearranging the terms in the resulting equation, we have

$$\begin{aligned}&\frac{\partial}{\partial t}\left(\frac{\partial u_i}{\partial x_j} + \frac{\partial u_j}{\partial x_i} - \frac{\partial u_l}{\partial x_i}\frac{\partial u_l}{\partial x_j}\right) + v_k \frac{\partial}{\partial x_k}\left(\frac{\partial u_i}{\partial x_j} + \frac{\partial u_j}{\partial x_i} - \frac{\partial u_l}{\partial x_j}\frac{\partial u_l}{\partial x_i}\right) + \frac{\partial v_k}{\partial x_j}\left(\frac{\partial u_i}{\partial x_k} + \frac{\partial u_k}{\partial x_i} - \frac{\partial u_l}{\partial x_k}\frac{\partial u_l}{\partial x_i}\right) + \frac{\partial v_k}{\partial x_i}\left(\frac{\partial u_j}{\partial x_k} + \frac{\partial u_k}{\partial x_j} - \frac{\partial u_l}{\partial x_k}\frac{\partial u_l}{\partial x_j}\right)\\ &\quad = \frac{\partial v_i}{\partial x_j} + \frac{\partial v_j}{\partial x_i}.\end{aligned} \tag{A.5}$$

Notice that

$$\frac{1}{2}\left(\frac{\partial u_i}{\partial x_j}+\frac{\partial u_j}{\partial x_i}-\frac{\partial u_l}{\partial x_i}\frac{\partial u_l}{\partial x_j}\right)=S_{ij} \tag{A.6}$$

is the *Almansi* strain tensor. Therefore, we get

$$\frac{\partial S_{ij}}{\partial t}+v_k\frac{\partial S_{ij}}{\partial x_k}+S_{ik}\frac{\partial v_k}{\partial x_j}+\frac{\partial v_k}{\partial x_i}S_{kj}=\frac{1}{2}\left(\frac{\partial v_i}{\partial x_j}+\frac{\partial v_j}{\partial x_i}\right). \tag{A.7}$$

Appendix B. Zeroth order solution for the extra stress and pressure inside the solid

In this section, we solve the 0*th* extra stress tensor from the constitutive equations in the solid. The component form of Eq. (39) for τ^0 in the cylindrical coordinates reads

$$\frac{D\tau_{rr}}{Dt}-2\frac{v_\theta^0}{r}\tau_{r\theta}+2\left(\frac{\partial v_r^0}{\partial r}\tau_{rr}+\frac{\partial v_\theta^0}{\partial r}\tau_{r\theta}\right)=2\frac{\partial v_r^1}{\partial r}, \tag{B.1}$$

$$\frac{D\tau_{\theta\theta}}{Dt}+2\frac{v_\theta^0}{r}\tau_{r\theta}+2\left(\left(\frac{1}{r}\frac{\partial v_r^0}{\partial\theta}-\frac{v_\theta^0}{r}\right)\tau_{r\theta}+\left(\frac{1}{r}\frac{\partial v_\theta^0}{\partial\theta}+\frac{v_r^0}{r}\right)\tau_{\theta\theta}\right)=2\left(\frac{1}{r}\frac{\partial v_\theta^1}{\partial\theta}+\frac{v_r^1}{r}\right), \tag{B.2}$$

$$\frac{D\tau_{r\theta}}{Dt}+\frac{v_\theta^0}{r}(\tau_{rr}-\tau_{\theta\theta})+\left(\frac{\partial v_r^0}{\partial r}+\frac{1}{r}\frac{\partial v_\theta^0}{\partial\theta}+\frac{v_r^0}{r}\right)\tau_{r\theta}+\left(\frac{1}{r}\frac{\partial v_r^0}{\partial\theta}-\frac{\partial v_\theta^0}{\partial r}\right)\tau_{rr}+\frac{\partial v_\theta^0}{\partial r}\tau_{\theta\theta}=\frac{1}{r}\frac{\partial v_r^1}{\partial\theta}+\frac{\partial v_\theta^1}{\partial r}-\frac{\partial v_\theta^1}{\partial r}, \tag{B.3}$$

where the material derivative is defined by $\frac{D}{Dt}=\frac{\partial}{\partial t}+v_r^0\frac{\partial}{\partial r}+\frac{v_\theta^0}{r}\frac{\partial}{\partial\theta}$. Using the 0*th* order velocity solution $\mathbf{v}^0=-\frac{1}{2}r\mathbf{e}_\theta$ for a freely rotating cylinder and at the steady state, Eqs. (B.1)–(B.3) reduce to

$$-\frac{1}{2}\frac{\partial\tau_{rr}}{\partial\theta}=2\frac{\partial v_r^1}{\partial r}, \tag{B.4}$$

$$-\frac{1}{2}\frac{\partial\tau_{\theta\theta}}{\partial\theta}=2\left(\frac{1}{r}\frac{\partial v_\theta^1}{\partial\theta}+\frac{v_r^1}{r}\right), \tag{B.5}$$

$$-\frac{1}{2}\frac{\partial\tau_{r\theta}}{\partial\theta}=\frac{1}{r}\frac{\partial v_r^1}{\partial\theta}+\frac{\partial v_\theta^1}{\partial r}-\frac{\partial v_\theta^1}{\partial r}. \tag{B.6}$$

Since the incompressibility requires that $\nabla\cdot\mathbf{v}^1=\frac{1}{r}\frac{\partial(rv_r^1)}{\partial r}+\frac{1}{r}\frac{\partial v_\theta^1}{\partial\theta}=0$, we can further simplify Eqs. (B.4)–(B.6) as

$$\frac{\partial\tau_{rr}}{\partial\theta}=-4\frac{\partial v_r^1}{\partial r}, \tag{B.7}$$

$$\frac{\partial\tau_{r\theta}}{\partial\theta}=-2\left(\frac{1}{r}\frac{\partial v_r^1}{\partial\theta}+\frac{\partial v_\theta^1}{\partial r}-\frac{\partial v_\theta^1}{\partial r}\right), \tag{B.8}$$

$$\tau_{rr}+\tau_{\theta\theta}=0. \tag{B.9}$$

Now putting the 1*st* order velocity solution of Eq. (41) into Eqs. (B.7) and (B.8), we find

$$\tau_{rr}=-\tau_{\theta\theta}=A(r)-2c_1\sin 2\theta+(c_2+c_3)\cos 2\theta, \tag{B.10}$$

$$\tau_{r\theta}=B(r)-2c_1\cos 2\theta-(c_2+c_3)\sin 2\theta. \tag{B.11}$$

Using the solutions τ^0 from Eqs. (B.10) and (B.11), we can also solve p^0 from Eq. (38) which reduces to

$$\frac{\partial p^0}{\partial r}=\frac{\partial\tau_{rr}}{\partial r}+\frac{1}{r}\frac{\partial\tau_{r\theta}}{\partial\theta}+\frac{2}{r}\tau_{rr}=A'+\frac{2}{r}A, \tag{B.12}$$

$$\frac{1}{r}\frac{\partial p^0}{\partial\theta}=\frac{\partial\tau_{r\theta}}{\partial r}-\frac{1}{r}\frac{\partial\tau_{rr}}{\partial\theta}+\frac{2}{r}\tau_{r\theta}=B'+\frac{2}{r}B \tag{B.13}$$

with the periodic boundary condition $p^0(r,\theta+2\pi)=p^0(r,\theta)$. The solution to Eqs. (B.12) and (B.13) takes the form

$$p^0=G(r), \tag{B.14}$$

where $G(r)$ and $A(r)$ are related by $G'=A'+2A/r$. The periodic boundary condition requires $B(r)=B_0/r^2$. Due to the fact that the stress has to be finite inside the particle, we have $B_0=0$.

References

[1] H.H. Hu, Direct simulation of flows of solid–liquid mixtures, Int. J. Multiphase Flow 22 (1996) 335–352.

[2] J.J. Feng, P. Huang, D.D. Joseph, Dynamic simulation of sedimentation of solid particles in an Oldroyd-B fluid, J. Non-Newtonian Fluid Mech. 26 (1996) 63–88.

[3] H.H. Hu, M.Y. Zhu, N. Patankar, Direct numerical simulations of fluid solid systems using the arbitrary Lagrangian Eulerian technique, J. Comput. Phys. 169 (2001) 427–462.

[4] U. Seifert, Configurations of fluid membranes and vesicles, Adv. Phys. 46 (1997) 13–137.

[5] H.A. Stone, Drop deformation and breakup in viscous flows, Annu. Rev. Fluid Mech. 26 (1994) 65–1021.

[6] A.B. Subramaniam, M. Abkarian, L. Mahadevan, H.A. Stone, Non-spherical gas bubbles, Nature 438 (2005) 930.

[7] C.S. Peskin, Flow patterns around heart valves: a numerical method, J. Comput. Phys. 10 (1972) 252–271.

[8] C.S. Peskin, The immersed boundary method, Acta Numerica 10 (2002) 479–517.

[9] T. Ye, R. Mittal, H.S. Udaykumar, W. Shyy, An accurate Cartesian grid method for viscous incompressible flows with complex immersed boundaries, J. Comput. Phys. 156 (1999) 209–240.

[10] R.J. LeVeque, Z. Li, The immersed interface method for elliptic equations with discontinuous coefficients and singular sources, SIAM J. Num. Anal. 31 (1994) 1019–1044.

[11] L. Zhang, A. Gerstenberger, X. Wang, W.K. Liu, Immersed finite element method, Comput. Methods Appl. Mech. Eng. 193 (2004) 2051–2067.

[12] R. Mittal, G. Iaccarino, Immersed boundary methods, Annu. Rev. Fluid Mech. 37 (2005) 239–261.

[13] C.W. Hirt, A.A. Amsden, J.L. Cook, An arbitrary Lagrangian–Eulerian computing method for all flow speeds, J. Comput. Phys. 14 (1974) 227–253.

[14] T.E. Tezduyar, M. Behr, J. Liou, A new strategy for finite element computation involving moving boundaries and interfaces – the deforming-spatial-domain/space-time procedure: I. The concept and the preliminary numerical tests, Comput. Meth. Appl. Mech. Eng. 94 (1992) 339–351.

[15] A. Masud, T.J.R. Hughes, A space-time Galerkin/least-squares finite element formulation of the Navier–Stokes equations for moving domain problems, Comput. Meth. Appl. Mech. Eng. 146 (1997) 91–126.

[16] C. Farhat, M. Lesoinne, Two efficient staggered algorithms for the serial and parallel solution of three-dimensional nonlinear transient aeroelastic problems, Comput. Meth. Appl. Mech. Eng. 182 (2000) 499–515.

[17] V. Kalro, T.E. Tezduyar, A parallel 3D computational method for fluid–structure interactions in parachute systems, Comput. Meth. Appl. Mech. Eng. 190 (2000) 321–332.

[18] P. Le Tallec, J. Mouro, Fluid structure interaction with large structural displacements, Comput. Meth. Appl. Mech. Eng. 190 (2001) 3039–3067.

[19] B. Hübner, E. Walhorn, D. Dinkler, A monolithic approach to fluid–structure interaction using space-time finite elements, Comput. Meth. Appl. Mech. Eng. 193 (2004) 2087–2104.

[20] F.J. Blom, A monolithical fluid–structure interaction algorithm applied to the piston problem, Comput. Meth. Appl. Mech. Eng. 167 (1998) 369–391.

[21] T.M. Fischer, M. Stöhr-Liesen, H. Schmid-Schönbein, The red cell as a fluid droplet: tank tread-like motion of the human erythrocyte membrane in shear flow, Science 202 (1978) 894–896.

[22] S. Chien, Red cell deformability and its relevance to blood flow, Annals Rev. Physiol. 49 (1987) 177–192.

[23] D. Barthěs-Biesel, Motion of a spherical microcapsule freely suspended in a linear shear flow, J. Fluid Mech. 100 (1980) 831–853.

[24] D. Barthěs-Biesel, J.M. Rallison, The time-dependent deformation of a capsule freely suspended in a linear shear flow, J. Fluid Mech. 113 (1981) 251–267.

[25] S.R. Keller, R. Skalak, Motion of a tank-treading ellipsoidal particle in a shear flow, J. Fluid Mech. 120 (1982) 27–47.

[26] C.D. Eggleton, A.S. Popel, Large deformation of red blood cell ghosts in a simple shear flow, Phys. Fluids 10 (1998) 1834–1845.

[27] H. Zhou, C. Pozrikidis, Deformation of liquid capsules with incompressible interfaces in simple shear flow, J. Fluid Mech. 283 (1982) 175–200.

[28] S. Ramanujan, C. Pozrikidis, Deformation of liquid capsules enclosed by elastic membranes in simple shear flow: large deformations and the effect of capsule viscosity, J. Fluid Mech. 361 (1998) 117–143.

[29] C. Pozrikidis, Numerical simulation of the flow-induced deformation of red blood cells, Annals Biomed. Eng. 31 (2003) 1194–1205.

[30] Y. Sui, Y.T. Chew, P. Roy, H.T. Low, A hybrid method to study flow-induced deformation of three-dimensional capsules, J. Comput. Phys. 227 (2008) 6351–6371.

[31] R.B. Bird, R.C. Armstrong, O. Hassager, Dynamics of polymeric liquids, Fluid Mech., vol. 1, John Wiley & Sons, New York, 1987.

[32] D.D. Joseph, Fluid dynamics of viscoelastic liquids, Appl. Math. Sci., vol. 84, Springer Verlag, New York, 1990.

[33] J.G. Oldroyd, Non-Newtonian effects in steady motion of some idealized elastico-viscous liquids, Proc. R. Soc. Lond. A 245 (1958) 278–297.

[34] F. Thomasset, Implementation of Finite Element Methods for Navier–Stokes Equations, Springer Verlag, New York, 1981.

[35] Y. Saad, Y. Schultz, GMRES: a generalized minimal residual algorithm for solving nonsymmetric linear systems, SIAM J. Sci. Stat. Comput. 7 (1986) 856–869.

[36] E. Chow, Y. Saad, Experimental study of ILU preconditioners for indefinite matrices, J. Comput. Appl. Math. 86 (1997) 387–414.

[37] S.P. Timoshenko, J.N. Goodier, Theory of Elasticity, third ed., McGraw Hill, New York, 1970.

[38] G.I. Taylor, The viscosity of a fluid containing small drops of another fluid, Proc. R. Soc. Lond. A 138 (1932) 41–48.

[39] W.J. Milliken, L.G. Leal, Deformation and breakup of viscoelastic drops in plannar extensional flows, J. Non-Newtonian Fluid Mech. 40 (1991) 355–379.

[40] F.P. Bretherton, The motion of rigid particles in a shear flow at low Reynolds number, J. Fluid Mech. 14 (1962) 284–304.